HHS Public Access

Author manuscript

J Biophotonics. Author manuscript; available in PMC 2019 August 01.

Published in final edited form as:

J Biophotonics. 2018 August ; 11(8): e201700017. doi:10.1002/jbio.201700017.

Simultaneous measurements of lymphatic vessel contraction, flow and valve dynamics in multiple lymphangions using optical coherence tomography

Cedric Blatter[1,3,§], **Eelco F.J. Meijer**[2,3,§], **Timothy P. Padera**[2,3,‡], and **Benjamin J. Vakoc**[1,3,‡,*]

[1]Wellman Center for Photomedicine, Massachusetts General Hospital, Boston, Massachusetts 02114, USA

[2]Edwin L. Steele Laboratories for Tumor Biology, Department of Radiation Oncology, Massachusetts General Hospital Cancer Center, Boston, Massachusetts 02114, USA

[3]Harvard Medical School, Boston, Massachusetts 02115, USA

Abstract

Lymphatic dysfunction is involved in many diseases including lymphedema, hypertension, autoimmune responses, graft rejection, atherosclerosis, microbial infections, cancer and cancer metastasis. Expanding our knowledge of lymphatic system function can lead to a better understanding of these disease processes and improve treatment options. Here, optical coherence tomography (OCT) methods were used to reveal intraluminal valve dynamics in 3D, and measure lymph flow and vessel contraction simultaneously in three neighboring lymphangions of the afferent collecting lymphatic vessels to the popliteal lymph node in mice. Flow measurements were based on Doppler OCT techniques in combination with exogenous lymph labelling by Intralipid. Through these imaging methods, it is possible to study lymphatic function and pumping more comprehensively. These capabilities can lead to a better understanding of the regulation and dysregulation of lymphatic vessels in health and disease.

Graphical Abstract

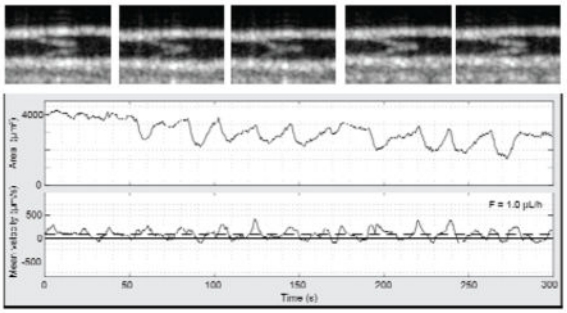

Dynamic measurements of lymphatic valves, lymphatic vessels cross-sectional area and lymph velocity simultaneously measured *in vivo* with optical coherence tomography.

*Correspondence and requests for materials should be addressed to (bvakoc@mgh.harvard.edu).

§, ‡Authors contributed equally.

Dysfunction of the lymphatic system plays a role in many disease processes, including lymphedema, hypertension, microbial infections and cancer. Expanding our knowledge of lymphatic system function can lead to a better understanding of these disease processes and improve treatment options. Here, the first measurements to characterize lymphatic vessel function in multiple segments were made in a living animal to begin to unravel how the lymphatic system is coordinated in normal and disease settings.

Keywords

optical coherence tomography; lymphatic vessel; flow velocity

Introduction

The lymphatic system is critical for maintaining tissue fluid balance, generating adaptive immune responses and carrying lipids absorbed in the gut to the blood circulation. Consequently, lymphatic impairment can lead to tissue swelling, immune dysfunction and gut malabsorption. Moreover, a large array of diseases is related to lymphatic dysfunction including lymphedema, hypertension, autoimmune responses, graft rejection, atherosclerosis, microbial infections, cancer and cancer metastasis [1]. Therefore, expanding our knowledge of normal lymphatic function, as well as lymphatic dysfunction in disease settings, is of paramount importance to understanding these pathologies and exploring new treatment options.

The lymphatic system consists of lymph nodes, an extensive network of lymphatic vessels and circulating lymph. Lymph enters the system through a network of initial lymphatic vessels embedded in tissue (Fig. 1a). These initial lymphatics feed into a network of larger pre-collecting and collecting vessels that drain to lymph nodes, where systemic immune responses are initiated. After exiting lymph nodes, lymph is transported to the venous angles in the neck where it returns to the systemic circulation [2]. The lymphatic collecting vessels primarily serve to actively transport lymph along this route, often against external forces. This active pumping of lymph is achieved by a combination of lymphatic contractions—both active and passive—that force lymph forward, and intraluminal valves that prevent net backflow. This action is distributed along a collecting lymphatic vessel, which comprises a series of lymphangions—the segments between two valves. Each lymphangion is invested by lymphatic muscle cells [3] to provide contraction forces. Through the coordinated contraction of multiple lymphangions, lymph flow is driven forward [4]. However, the nature and mechanisms for lymphangion coordination and valve action in normal states, or the disruption of this coordination in disease states are not well understood.

To deepen the understanding of lymphatic function, lymphatic imaging technologies have been developed and deployed in preclinical and clinical settings. In the clinic, lymphoscintigraphy [5, 6] and near infrared (NIR) fluorescence imaging [7] have been used to assess the severity of lymphatic dysfunction. MRI [8] and CT [9] provide more information regarding anatomical status for treatment planning, for example in treating advanced lymphedema. In preclinical settings, *ex vivo* experiments [10, 11] and

computational modelling [4, 12] have given great insight into the behavior of lymphatic valves and lymphangions and their possible functioning *in vivo*. Lymphatic pumping frequency has been assessed non-invasively with NIR fluorescence imaging [13–15]. To provide higher-resolution imaging of lymphatic vessels, fluorescence microscopy (FM) can be used after surgical removal of overlying skin. This method has been used to resolve the diameter change of the lymphatic vessel with each contraction and visualizing valve action [13, 16]. Optical coherence tomography (OCT) provides label-free three-dimensional (3D) imaging of tissue scattering at micron-scale resolutions. The optical biopsy capability of OCT has been successfully demonstrated for imaging lymph nodes [17–20]. The scattering difference between the relatively acellular lymph and the surrounding tissue has been used as a contrast mechanism to image the lymphatic network [21–27]. While these techniques provide insight into specific aspects of lymphatic function, they are unable to directly assess lymph flow.

Doppler OCT (DOCT) analyzes scattering signals over time to measure motion along the optical beam [28]. Recently, we developed an *in vivo* label-free method to measure lymph flow velocity and volumetric flow rates using DOCT [29]. Using this method, we are able to resolve (pulsatile) lymph flow at a single location within afferent popliteal collecting lymphatic vessels in the mouse hindlimb. We demonstrated two different imaging modes over time: single spatial depth-resolved measurement (M-scan) and cross-sectional imaging (B-scan). The latter has the advantage of providing intraluminal flow velocity profiles, vessel contractile activity by segmentation of the vessel in a series of repeated measurement, and volumetric flow rate by multiplication of the mean velocity with the segmented lumen.

To date, no *in vivo* method has been demonstrated that allows investigation of how lymphangion contractions and lymphatic valves cooperate to drive lymph flow with direct measurements of each of these three parameters. Here, we extend the OCT/DOCT technique to support the simultaneous measurement of flow and contraction in neighboring lymphangions and the status (i.e., open vs closed) of the adjoining valves. In addition, we show that injection of Intralipid can be used to increase the OCT signal within the vessel to improve temporal sampling of the flow velocity. We use this system to measure these parameters in three adjacent lymphangions in a normal mouse and in a model of sterile inflammation. This method will allow the study of the synchrony between lymph flow, valve dynamics and lymphatic contraction to better understand the regulation and dysregulation of lymphatic vessels in health and disease.

Materials & methods

Animal preparation

We used 8 to 16-week-old C3H male mice (26–36 g) for all experiments. Before surgery, mice were anaesthetized using a ketamine/xylazine mixture at 100mg/10mg per kg body weight. The surgical procedure was performed as described previously [30, 31]. Briefly, after hair removal, the skin on the dorsal side of the mouse hindlimb was surgically removed to expose the primary artery/vein pair. The lymphatic vessels run approximately parallel to these blood vessels. Exposed tissue was kept hydrated using physiological saline. After surgery, mice were positioned on a stage tilted 15 degrees with the blood vessel along the

maximum slope direction and the body at a higher elevation than the hindlimb. Surgical tape was then used to secure the hindlimb. The 15-degree angle provides a gravity induced opposing pressure as would normally be felt in the hindlimb of an ambulating mouse. The footpad was then injected with 10 μL of Intralipid (Sigma-Aldrich) diluted at either 1:5 or 1:10 with water. We adjusted the dilution to be 1:5 in the normal mouse and 1:10 in the inflammation model experiment to better preserve the contrast between fluid and intraluminal valves. The diluted Intralipid was used to increase the OCT signal within the vessel and improve lymph velocity measurement quality. As described in Liao et al. [30], skin contact sensitization using oxazolone induces sterile cutaneous inflammation which peaks on day 4 and resolves spontaneously by day 7. Therefore, for the oxazolone experiments, four days before imaging, 50 μL of 4% oxazolone (Sigma-Aldrich) in acetone was applied topically to the skin area on the dorsal side of each leg after hair removal. Care was taken to avoid application of oxazalone to skin over the paw. Mice were euthanized at the end of the imaging session. The animal experiment protocol was reviewed and approved by Institutional Animal Care and Use Committee of the Massachusetts General Hospital. The procedures were performed in accordance with the approved guidelines.

DOCT system

The OCT system is similar to that described in prior work [29]. The system uses a swept-wavelength laser source centered at ~1300 nm with an A-scan rate of 50 kHz. The full optical bandwidth of 100 nm provides an axial resolution of 5.3 μm in tissue. The sensitivity is ~105 dB with 10 mW on the sample. Phase instability, typically present with kinetic swept sources and phase unlocked electronics, is corrected in post-processing by using reference signals from fixed delay reflections [29]. A pair of galvanometer-based optical scanners (Cambridge Technology) steer the beam and define the coordinate system (x,y) together with the optical axis (z).

The beam path through the objective differs in the approach reported here from that described previously [29]. In that prior work, a Doppler angle (between the lymphatic vessel and the imaging beam) was generated by tilting the stage that supported the mouse. Creating the Doppler angle in this manner was adequate for measuring a single spatial point (M-scan) within a vessel or a cross-section (B-scan) orthogonal to its flow direction. However, because of the short depth of focus, this approach fails when measuring at several locations along the vessel. To circumvent this issue, a Doppler angle α is obtained by a shift (Δy) of the beam from the optical axis in the back aperture of the objective (Fig. 1b). The beam was collimated to 2.8 mm, which underfills the pupil plane of the objective lens (LSM02, Thorlabs). A shift of 2.3 mm produces a focused beam departing from the optical axis at 7.3 degrees resulting in a Doppler angle of 82.7 degrees for a vessel lying in the focus plane.

The selection of the imaging Doppler angle is a design trade-off. Smaller values, further from 90 degrees, yield increased accuracy in velocity measurements but require operating further from the objective center axis, which increases aberrations and reduces transverse resolution. The design chosen shows reasonable optical performance over a distance of ±2 mm along the y axis —sufficient to cover the typical length of more than two complete lymphangions at the region of interest— as simulated by a ray tracing program (Zemax). In

addition, although a smaller Doppler angle might provide potentially lower velocity accuracy, the current value still allows a correct measurement of event timing (zero crossings, maxima, minima) and therefore the study of the synchronicity between measurement locations.

Imaging procedure

The stage was rotated to align the hindlimb primary artery/vein pair to the *y*-direction of the galvanometer pair. The lymphatic vessel was identified from real-time OCT B-scan images, with the fast axis scanning direction along *x*-axis and the slow axis amplitude set to zero along the *y*-axis. The vessel was centered in the field of view by translation of the stage. Alternating fast and slow axis scanning between *y* and *x* allows imaging along the vessel (Fig. 1c), which enables low scattering structures such as fat cells to be distinguished from the lymphatic vessel, as well as identification of intraluminal valves. The rotation of the stage is then adjusted to maximize the length of the lymphatic vessel visible in the field of view. Finally, the stage is translated in the *y*-direction to a chosen position. During the imaging session, tissue was kept hydrated by topical application of physiological saline.

At the end of each measurement, a volume spanning a 1.4 × 2.1 mm scanning area (464 A-scans per B-scans, 464 B-scans) was acquired. These volumes were analyzed to display the tissue surrounding the measurement locations and to extract the vessel, tissue and air boundaries (Fig. 1c) in order to calculate the vessel Doppler angle at each flow measurement location as previously described [29]. The measured vessel Doppler angle can be different from the set value because of the anatomical position of the vessel within the leg.

DOCT Processing

Standard processing algorithms were used to obtain complex depth-resolved scattering profiles, or A-scans, from raw interferometric fringes as previously described [29, 33]. The data was corrected for tissue bulk motion by manually selecting a region of tissue whose temporal phase evolution was later subtracted from the rest of the dataset. The temporal power spectral density was calculated over every group of 32 repeated B-scans for each spatial pixel. It was then fitted by two constrained circular Gaussians and a white noise background, the first one centered at 0 Hz representing tissue and the second Gaussian shifted from 0 Hz estimating the Doppler frequency shift by its center. Wrapping artifacts, showing pixels of backward velocities within forward flow pulses or vice versa, sometimes appeared during high flow pulses because of the limited frame rate. We have improved our unwrapping methods from our previous approach by examining the temporal evolution of the averaged velocity at each depth within the vessel. Points of forward velocity during backward pulses and vice versa were unwrapped to the corresponding direction. The unwrapped frequency was finally converted to the flow velocity with knowledge of the vessel Doppler angle.

The lymphatic vessel was automatically segmented based on the intensity contrast between lymph and surrounding tissue using a 2D snake algorithm [34] that operates by using the mean of the 32 B-scans. The vessel segmented area was obtained from the surface of the polygon defined by the contour points. The surface measured in the imaging plane is finally

rescaled by the cosine of the Doppler angle to obtain the vessel area. All the processing was performed automatically except for the Doppler angle measurement which was manually retrieved from the imaging volume.

Results

4D OCT reveals lymphatic valve dynamics

OCT imaging can resolve intraluminal valves in collecting lymphatic vessels. A valve was measured over five minutes, which corresponds to 1084 volumes, each of 144 A-scans by 96 B-scans, to image its dynamics (Fig. 2, Supplementary Movie 1). Figure 2a–f show cross-sections of the lymphatic vessel at an intraluminal valve. The images on the left in each panel show cross-sections perpendicular to the vessel that clearly show the angular orientation of the valve. On the right, the view along the vessel shows the valve flaps. Valve closing took less than 0.56 seconds and the valve remained closed for about 6 seconds. The valve reopened in less than 0.28 seconds, which is the temporal resolution of this scanning protocol. 3D rendering views extracted from the 4D dataset show the valve in open and closed positions (Fig. 2g–h). 4D datasets of valve closings allow simultaneous lymphatic vessel contractions and valve closings to be observed (Supplementary movie 2).

Intralipid injection increases lymph scattering and allows more rapid measurement of lymph flow

Scattering from lymph is very low, but its OCT signal can still be detected [29]. To enable the measurement of lymph flow using the native lymph signal, long acquisition times are necessary, making it challenging to simultaneously measure lymph flow at multiple locations. We show here that the injection of diluted Intralipid increases the OCT signal strength of the fluid within the lymphatic vessel lumen and enables simultaneous flow measurements using DOCT. Figure 3 shows the scattering intensity of lymph before and after injection of Intralipid. Signal-to-noise ratio (SNR) values were measured as the ratio between the average value of pixels within the vessel and the average value of noise pixels. Both regions were manually selected. The comparison between pre- and post-injection of Intralipid in 5 mice shows an increase of 7 dB. This contrast enhancement allows an increased precision of the velocity measurement (Fig. 3d) and is sufficient to measure flow at several locations while maintaining enough temporal resolution to resolve flow dynamics at each of these locations. The standard deviation was evaluated at times between flow peaks, when the velocity is almost constant. The standard deviation of 31 μm/s with Intralipid is typical of the precision obtained on the mean velocity at each time point for the results presented in the rest of manuscript. The addition of Intralipid improves the flow velocity peak discrimination. Although the time-average velocity might change after Intralipid injection, the coordination between contractions, valve status and pulsatile flow can still be studied. Importantly, Intralipid at the dilutions used in these experiments preserves the contrast between lymph and valves that is necessary to resolve closing events.

Lymph flow, lymphatic vessel contraction and lymph valve dynamics can be imaged simultaneously across multiple lymphangions

We next performed experiments to demonstrate the feasibility of measuring lymphatic vessel contraction, flow velocity and volumetric flow rate simultaneously within three contiguous lymphangions, from distal to proximal, along with the motion of the two intervening valves (Fig. 4). The stage was moved to a position approximately equidistant to two intraluminal valves, with the lymphatic vessel parallel to the *y*-axis. Repeated B-scans in three successive lymphangions for flow and contraction measurements, as well as 4D data for the two intervening valves are acquired sequentially using their *y* coordinates (Fig. 4a). A smaller Doppler angle reduces the range of the Doppler frequency shifts for a given flow velocity range. As a result, the frame rate could be reduced (compared to our previous work [29]) to capture this smaller frequency shift. This allows for a better lateral spatial sampling at a fixed A-scan rate. In addition, the amount of repetition at each location is a trade-off between sufficient B-scans—for precise measurement of the Doppler frequency shift and the spatial sampling for valve imaging—and sufficient temporal resolution to measure the dynamics of velocity pulses, which typically last for few seconds and occur every 15–20 seconds in healthy mice [29]. We designed the scanning protocol for a five-minute measurement composed of 697 temporal points in total. Each temporal point consists of 32 B-scans at each flow measurement location (constant slow axis signal) and a volume consisting of 64 B-scans spread over a constant length of ~150 μm at each valve location (ramp slow axis signal). The duration of a single time point comprising all of these measurements is 430 ms, which is short compared to the lymphatic flow and contractile dynamics. The measurement over locations is therefore considered to be effectively simultaneous. A ramp waveform with a period of 96 A-scans (~520Hz with the system A-scan frequency) was used to drive the fast axis galvo-scanner.

Figure 4b shows the locations of measurements in an *en face* plane through the lymphatic vessel. The vessel area and the mean cross-sectional velocity within the lymphangions, respectively at the top and bottom of each panel, and the status of the intervening valves are reported in Fig. 4c–g. The vessel area plots show clearly resolved contractions, which are identified by a slow increase of the vessel cross-section followed by a rapid decrease (*e.g.* black arrowhead in Fig. 4c). The curves of mean velocity, calculated as the average velocity over the vessel cross-section, show pulsatile activity. Positive mean flow velocities indicate flow in the proximal direction, while negative mean flow velocities indicate flow in the retrograde direction. The comparison between velocity and cross-sectional area shows that some velocity pulses occur during the contraction phase while others do not (Fig. 4, continuous and dashed vertical lines, respectively). The volumetric flow rate is calculated by multiplying the instantaneous mean cross-sectional velocity by the vessel cross-section. As expected, the average volumetric flow over the 300 s measurement is similar at the three locations. This is visible by comparing Fig. 4c and Fig. 4g, in which a smaller vessel area corresponds to higher velocity. The comparison of the three locations shows that the velocity pulses are synchronous (Fig. 4, continuous and dashed vertical lines). The velocity curves correlate well and have the same number of pulses (3.2 peaks per minute). The curves plotting cross-sectional area show simultaneous contractions. The number of contractions, quantified manually and defined in a moving averaged curve as an area change from peak to

valley larger than 10%, are 1.8, 1.6 and 1.4 contractions per minute for Fig. 4c, e and g respectively.

Valve activity was manually measured from the 4D datasets. In the example in Fig. 4, the more distal valve closed once during the measurement (Fig. 4d, ellipse), when the vessel area was the smallest at all locations, while the proximal valve stayed open during the entire five-minute measurement (Fig. 4f). The closing occurs at the end of a vessel contraction in the distal lymphangion and when the velocity transitions from positive to negative at all locations. During the closing, the velocity maintains its retrograde direction at all locations. The cross-section remains minimum at the distal and proximal location, while it increases in the intermediate lymphangion. When the valve re-opens, the cross-sectional area at the distal and proximal locations increases, and continues to increase at the intermediate location. At the same time, the velocity becomes positive. The increase of the cross-section of the intermediate lymphangion agrees with the negative flow in front of the closed valve. There are multiple other time points in the five-minute dataset when the velocities show a similar profile but the valve did not close.

In our measurements, we observed an initial period of low contractile amplitude and a slow trend of decreasing vessel cross-sectional area. This could be attributable to a combination of the surgery, the between-measurement addition of saline, the transient increase in intraluminal pressure due to the injection of Intralipid or the presence of Intralipid itself.

Lymph flow, contraction and valve dynamics in sterile inflammation

We performed simultaneous measurements of lymph flow and valve dynamics in a mouse after exposure to oxazolone (Fig. 5). The accuracy and precision of the mean velocity and average flow are limited at the distal and intermediate locations in this measurement because of a vessel Doppler angle close to 90 degrees at those locations. To improve the visualization of the data, the velocity measurement (black points) were smoothed with a moving average of four points (solid line). In this example, the lymphatic vessel cross-section shows about 5.8, 6 and 3.4 contractions per minute for Fig. 5a, c and e respectively, quantified manually and defined in a moving average curve as an area change from peak to valley larger than 10%. The velocity shows an oscillation pattern with forward and back flow, but with a net positive forward average. The mean velocity at the intermediate and proximal locations is similar although the velocity amplitudes at the latter location is larger. The velocity curves are synchronous at the intermediate and proximal locations, but the typical contraction waveform is absent. However, the velocity curves are synchronous with the distal location only after about 130 seconds. The apparent absence of synchronicity during the first 130 seconds could be caused by animal motion which changed the measurement location and thereby the flow direction seen by the optical beam. This could also explain the changes in velocity at the beginning of the measurement. Nonetheless, this measurement shows interesting valve activity. All seven valve closing events correspond to the crossing from forward to backward velocity, but not all directional flow changes correspond to a closing event. Because of the limited velocity accuracy and precision due to the large Doppler angle, we limit our description to the more proximal valve. When this valve is closing, the magnitude of the backward velocity at the proximal location decreases and becomes zero,

with a form similar to a negative exponential (Fig. 5, ellipse). When the valve opens, the flow velocity increases in the proximal direction as fluid moves forward. Valve closings occur at the end of a distal vessel contraction.

Previous work has reported attenuated lymphatic pumping and significantly increased vessel diameters after oxazolone treatment in mice [12, 30]. Using fluorescence microscopy, two phenotypes of lymphatic contraction in the collecting lymphatic vessel leading to the popliteal lymph node were reported four days after oxazolone skin painting. One phenotype showed absent or low contraction frequency. The other showed a higher frequency with a very small amplitude. In the study from Liao *et al.*, the lymphatic contraction frequency after oxazolone skin painting increased from approximately 21 per min in controls to 32 per min on average in young C3H mice in which contractions were detected. We also measured a higher contraction frequency than normal in some oxazolone treated mice (e.g. Figure 5). Interestingly, a small forward flow is still maintained. Figure 6 shows a measurement in another oxazolone treated mouse, this time showing the other phenotype. In this example, the contraction activity is absent and the mean velocity is close to zero. Over all measurements, we see a clear difference in contraction frequencies, both for contraction and velocity, and mean velocity waveform between normal and oxazolone mice. Because of the different concentration of Intralipid used for control and inflamed mice, we cannot exclude that Intralipid had a differential effect on control and inflammation model mice. However, the higher concentration of Intralipid used in control, suggests that alterations caused by inflammation are greater than any effect of Intralipid on diminishing lymphatic vessel function [32].

Discussion

In this study, we developed a novel *in vivo* technique to simultaneously measure lymph flow and lymphatic vessel cross-sectional changes in three successive lymphangions, while also providing 4D imaging of the intervening lymphatic valves. We also demonstrated how Intralipid can be used to increase the OCT signal within the vessel, allowing for better temporal sampling of the flow velocity across multiple locations. In addition to the use of these methods in physiological settings, we demonstrated our technique in a mouse model of sterile inflammation. The difference between the number of contractions, flow peaks and average flow underscores the importance of measuring lymph flow when evaluating lymphatic function. Lymph flow is critical for fluid transport and antigen presentation to the lymph node.

The Intralipid injection, like dye injections in other methods used to measure lymphatic function, might perturb the physiological state of the lymphatic system. First, the injection itself might change the intraluminal pressure and alter the lymphatic function. With a different contrast agent injection, Weiler *et al.* have shown that there is a transient lymphatic pump function response occurring after a bolus injection that can take 5–10 minutes to reach steady state [35]. Second, acute high lipid loads have been shown to reduce lymphatic pump function in the rat mesentery model [32]. We therefore cannot exclude that there is a biological response to low concentrations of lipid introduced with diluted Intralipid. Nonetheless, in this study we sought to develop a method that can provide the most relevant

information about the synchronicity of lymphatic functional parameters (flow, valve dynamics and contractions) in multiple lymphangions. Therefore, we prioritized a better SNR by injecting a contrast agent and consequently were able to acquire nearly simultaneous B-scans in three lymphangions. Alternatively, it would be possible to use a non-lipid based scattering contrast agent to avoid a possible reaction of lymphatic vessels to lipid. Finally, if the interest lies in the study of physiology, a label-free approach, as previously shown [29], could be adopted at a cost of lower temporal resolution or fewer measurement locations.

There are opportunities to further improve the OCT system for this application. The current system provides moderate resolution and imaging speed. Higher resolution would allow a better definition of the valves. The valve tips can be particularly difficult to discriminate on the cross-sectional images. Isotropic sampling would also be advantageous to obtain similar cross-section quality for any valve angular orientation within the vessel. With current 6 μm axial and 11 μm transverse resolutions, the valves are best visualized in the depth-resolved cross-sections (y-z). This is complementary to microscopy where valves are visualized in the *en face* plane [16, 30, 36]. However, with OCT, we benefit from 3D views. Increasing the acquisition speed of the system would allow for a better sampling of the valve structure and the flow velocity profile, which may provide interesting information where two collecting lymphatic vessels conjoin. Alternatively, the temporal sampling could be increased to measure additional locations and prevent any Doppler frequency wrapping. Unwrapping can be a difficult task, especially with abnormal flow patterns that might occur in disease settings. Within the field of view where the optical quality of the beam is maintained, additional valve locations could be added. Using a larger field of view to assess additional locations would require a more complex optical system, such as adaptive focusing, to maintain the optical quality of the beam and the focusing, but might be ultimately limited by the use of a single objective. Our experience also suggests that it could be difficult to extend measurements to additional lymphangions in the mouse hindlimb because of the anatomical variation of these vessels. With our current approach, the lymphangions need to be well aligned and close to the surface. It would also be possible to add flow locations within the field of view if the SNR of the fluid can be maintained. Increasing the Intralipid concentration is technically easy and can be done in experiments dedicated to DOCT flow measurements alone, but for successful 4D valve measurements, the Intralipid concentration should be limited to preserve contrast between intraluminal fluid and valves.

Computational simulations have reproduced a range of behaviors observed in lymphatic vessels *in vivo* and *ex vivo* [4, 12, 37–42], aiding our comprehension of how lymphangions respond to mechanical cues as well as helping form hypotheses on the mechanisms behind lymphangion and valve coordination. Based on our *in vivo* experiments, we confirm that valves are biased-open and that valves may stay continuously open during pumping and retrograde flow, similar to what has been observed *ex vivo* [36]. In addition, we observe simultaneous contractions and flow peaks in the three successive lymphangions. Using Prox1-GFP mice and surgical exposure of the lymphatic vessel in the mouse flank, Chong *et al.*[16] were able to image vessel contraction and valve closing *in vivo*. Their data also show a relation between valve events and vessel cross-sectional changes. Similar to our observations, not every contraction correlated with a valve closing. Further studies are

needed to fully understand the synchronicity of valve function. Under our experimental conditions, valve closure is a rare event. It was seen in 2 of 6 healthy mice, and in only 4 out of about 55 five-minute valve measurements. In oxazolone treated mice, we observed valve closings in 1 of 6 mice and only in 2 out of 48 five-minute valve measurements.

Previous in vivo studies have reported changes to lymphatic vessel contraction frequency and amplitude after oxazolone induced inflammation, as well as a less common phenotype with highly dilated vessels and little vasomotion [12, 30]. While NO and Ca2+ influences on lymphatic vessel contraction have been extensively described in both physiology and pathophysiology, the complete mechanisms have not yet been unraveled. For example, little is known about endothelial mechanobiology and how shear stress signals are transduced [1].

The observation of open biased valves *in vivo* is an important element for numerical simulations as it narrows down possible scenarios. Valves stay open, possibly as a mechanism to minimize any impediment to flow in a chain of lymphangions [4]. The measurement of contractions could be performed on a larger number of animals to investigate the synchronization of contractions in detail. The current data suggest that they are synchronous to the eye or quasi-synchronous but do not exclude an occasional phase shift between successive lymphangions. This would be an important *in vivo* observation as it would help rule out possible explanations of local regulatory mechanisms [4]. Our method allows the *in vivo* study of physiology and pathology, including changes to lymphatic collecting vessels in the cancer (pre-)metastatic settings, after radiation therapy, after surgical interventions, and after *in vivo* gene knockdown (i.e. primary lymphedema and ion channel studies) as well as during therapeutic interventions.

Supplementary Material

Refer to Web version on PubMed Central for supplementary material.

Acknowledgments

Research reported in this publication was supported in part by the Center for Biomedical OCT Research and Translation through Grant Number P41EB015903, awarded by the National Institute of Biomedical Imaging and Bioengineering of the National Institutes of Health, by the National Institutes of Health under award numbers R01CA163528 (B.J.V.), DP2OD008780 (T.P.P.), R21AI097745 (T.P.P.) and R01HL128168 (T.P.P.). The National Cancer Institute Federal Share of Proton Income also supported this work (T.P.P., B.J.V.). Cedric Blatter was supported by a Swiss National Science Foundation early post-doctoral mobility fellowship (P2SKP2_158640). The authors acknowledge Lance L. Munn for the drawing of Figure 1a.

References

1. Padera TP, Meijer EF, Munn LL. Annual review of biomedical engineering. 2016
2. Schmid-Schonbein GW. Physiological reviews. 1990; 70:987–1028. [PubMed: 2217560]
3. Zawieja DC. Lymphatic research and biology. 2009; 7:87–96. [PubMed: 19534632]
4. Bertram CD, Macaskill C, Davis MJ, Moore JE Jr. American journal of physiology Heart and circulatory physiology. 2016; 310:H847–860. [PubMed: 26747501]
5. Mortimer PS, Rockson SG. The Journal of clinical investigation. 2014; 124:915–921. [PubMed: 24590276]
6. Brandon Dixon J, Weiler MJ. Seminars in cell & developmental biology. 2015; 38:75–82. [PubMed: 25545813]

7. Rasmussen JC, Kwon S, Sevick-Muraca EM, Cormier JN. Annals of biomedical engineering. 2012; 40:408–421. [PubMed: 22139396]
8. Liu N, Zhang Y. Journal of reconstructive microsurgery. 2014
9. Iimura T, Fukushima Y, Kumita S, Ogawa R, Hyakusoku H. Plastic and reconstructive surgery Global open. 2015; 3:e404. [PubMed: 26090294]
10. Gashev AA, Davis MJ, Delp MD, Zawieja DC. Microcirculation (New York, NY : 1994). 2004; 11:477–492.
11. Scallan JP, Davis MJ. The Journal of physiology. 2013; 591:2139–2156. [PubMed: 23420659]
12. Kunert C, Baish JW, Liao S, Padera TP, Munn LL. Proceedings of the National Academy of Sciences of the United States of America. 2015; 112:10938–10943. [PubMed: 26283382]
13. Kwon S, Sevick-Muraca EM. Journal of anesthesia. 2016; 30:1091–1094. [PubMed: 27730311]
14. Proulx ST, Luciani P, Derzsi S, Rinderknecht M, Mumprecht V, Leroux JC, Detmar M. Cancer Res. 2010; 70:7053–7062. [PubMed: 20823159]
15. Guo R, Zhou Q, Proulx ST, Wood R, Ji RC, Ritchlin CT, Pytowski B, Zhu Z, Wang YJ, Schwarz EM, Xing L. Arthritis and rheumatism. 2009; 60:2666–2676. [PubMed: 19714652]
16. Chong C, Scholkmann F, Bachmann SB, Luciani P, Leroux JC, Detmar M, Proulx ST. Scientific reports. 2016; 6:22930. [PubMed: 26960708]
17. McLaughlin RA, Scolaro L, Robbins P, Hamza S, Saunders C, Sampson DD. Cancer Res. 2010; 70:2579–2584. [PubMed: 20233873]
18. Luo W, Nguyen FT, Zysk AM, Ralston TS, Brockenbrough J, Marks DL, Oldenburg AL, Boppart SA. Technology in cancer research & treatment. 2005; 4:539–548. [PubMed: 16173824]
19. John R, Adie SG, Chaney EJ, Marjanovic M, Tangella KV, Boppart SA. Annals of surgical oncology. 2013; 20:3685–3693. [PubMed: 22688663]
20. Nguyen FT, Zysk AM, Chaney EJ, Adie SG, Kotynek JG, Oliphant UJ, Bellafiore FJ, Rowland KM, Johnson PA, Boppart SA. IEEE engineering in medicine and biology magazine : the quarterly magazine of the Engineering in Medicine & Biology Society. 2010; 29:63–70.
21. Qin W, Baran U, Wang R. Lasers in surgery and medicine. 2015; 47:669–676. [PubMed: 26224650]
22. Yousefi S, Qin J, Zhi Z, Wang RK. Journal of biomedical optics. 2013; 18:86004–86004. [PubMed: 23922124]
23. Zhi Z, Jung Y, Wang RK. Optics letters. 2012; 37:812–814. [PubMed: 22378402]
24. Jung Y, Zhi Z, Wang RK. Journal of biomedical optics. 2010; 15:050501. [PubMed: 21054073]
25. Vakoc BJ, Lanning RM, Tyrrell JA, Padera TP, Bartlett LA, Stylianopoulos T, Munn LL, Tearney GJ, Fukumura D, Jain RK, Bouma BE. Nature medicine. 2009; 15:1219–1223.
26. Baran U, Qin W, Qi X, Kalkan G, Wang RK. Scientific reports. 2016; 6:21122. [PubMed: 26892830]
27. Gong P, Es'haghian S, Harms KA, Murray A, Rea S, Wood FM, Sampson DD, McLaughlin RA. Biomedical optics express. 2016; 7:4886–4898. [PubMed: 28018713]
28. Leitgeb RA, Werkmeister RM, Blatter C, Schmetterer L. Progress in retinal and eye research. 2014; 41:26–43. [PubMed: 24704352]
29. Blatter C, Meijer EF, Nam AS, Jones D, Bouma BE, Padera TP, Vakoc BJ. Scientific reports. 2016; 6:29035. [PubMed: 27377852]
30. Liao S, Cheng G, Conner DA, Huang Y, Kucherlapati RS, Munn LL, Ruddle NH, Jain RK, Fukumura D, Padera TP. Proceedings of the National Academy of Sciences of the United States of America. 2011; 108:18784–18789. [PubMed: 22065738]
31. Liao S, Jones D, Cheng G, Padera TP. J Biol Methods. 2014; 1
32. Kassis T, Yarlagadda SC, Kohan AB, Tso P, Breedveld V, Dixon JB. American journal of physiology Gastrointestinal and liver physiology. 2016; 310:G776–789. [PubMed: 26968208]
33. Bouma BE, Yun SH, Vakoc BJ, Suter MJ, Tearney GJ. Current opinion in biotechnology. 2009; 20:111–118. [PubMed: 19264475]
34. Kass M, Witkin A, Terzopoulos D. International Journal of Computer Vision. 1988; 1:321–331.
35. Weiler M, Dixon JB. Frontiers in physiology. 2013; 4:215. [PubMed: 23966950]

36. Davis MJ, Rahbar E, Gashev AA, Zawieja DC, Moore JE. American Journal of Physiology - Heart and Circulatory Physiology. 2011; 301:H48–H60. [PubMed: 21460194]
37. Rahbar E, Moore JE Jr. Journal of biomechanics. 2011; 44:1001–1007. [PubMed: 21377158]
38. Wilson JT, Wang W, Hellerstedt AH, Zawieja DC, Moore JE. Journal of biomechanical engineering. 2013; 135:51005. [PubMed: 24231961]
39. Wilson JT, van Loon R, Wang W, Zawieja DC, Moore JE Jr. Journal of biomechanics. 2015; 48:3584–3590. [PubMed: 26315921]
40. Jamalian S, Davis MJ, Zawieja DC, Moore JE Jr. PloS one. 2016; 11:e0148384. [PubMed: 26845031]
41. Bertram CD, Macaskill C, Moore JE Jr. Medical engineering & physics. 2016; 38:656–663. [PubMed: 27185045]
42. Baish JW, Kunert C, Padera TP, Munn LL. PLoS computational biology. 2016; 12:e1005231. [PubMed: 27935958]

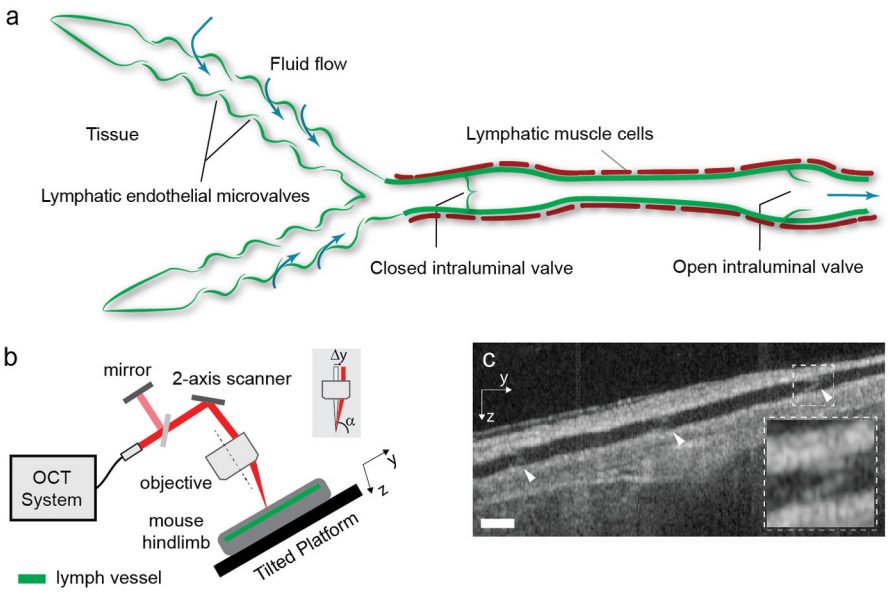

Figure 1.

Lymphatic imaging and flow measurement using Doppler OCT. (a) Anatomy of initial and collecting lymphatic vessels and valve function. Initial lymphatic vessels on the left collect interstitial fluid to create lymph, which is carried to a lymph node by a collecting lymphatic vessel. Lymphatic muscle cells can contract to drive flow, while intraluminal valves can close to prevent net backflow. The vessel segment between two valves is called a lymphangion. The figure is adapted with permission from Padera *et al.* [1]. (b) Schematic of the imaging setup. The light path is displayed in red. A portion of the collimated light is reflected to a mirror providing a reference signal for phase instabilities correction. A 2-axis galvanometer-based optical scanner is used to steer the beam. The beam shift (Δy) provides the Doppler angle α. The mouse is positioned with the lymphatic vessel along the *y* axis on a tilted platform with an angle of 15 degrees to provide a gravity induced opposing pressure gradient to lymph flow. The optical system has similar tilt to the tilted platform. (c) A cross-sectional image along the lymphatic vessel extracted from the volume data and used to calculate the Doppler angle at each flow location. Arrowheads point to intraluminal valves. Dashed region shows a close-up of a valve. Depending on their angular orientation within the vessel, the valves are better visualized in the cross-section or in the *en face* plane (Fig. 4b). Scale bars denote 130 μm.

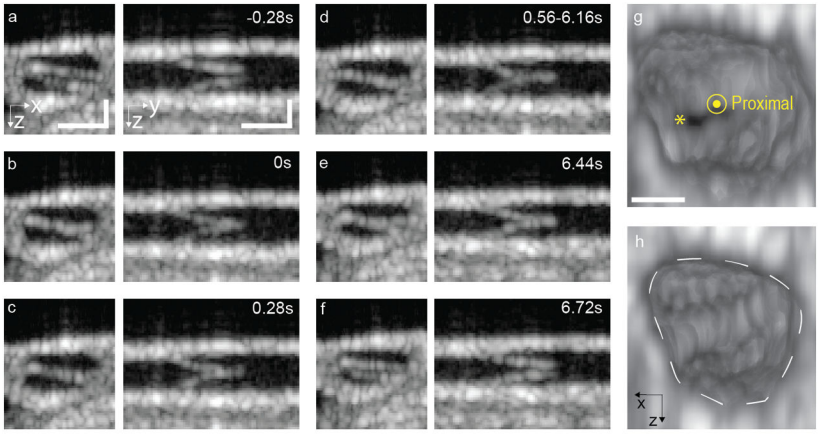

Figure 2.

4D imaging of valve dynamics. (a–f) Cross-sectional images perpendicular to and along the lymphatic vessel, on the left and right respectively. (c) An image was extracted from the 4D dataset at a time point when the valve is open. Time points of valve flaps (d) touching, (e) stronger contact, (f) valve closed, (g) valve initiating reopening and (h) opened. Scale bar denote 50 μm. The motion can be appreciated in Supplementary Movie 1. (g) and (h) 3D rendering of views extracted from the 4D dataset at a time when the valve is open (*) and closed, respectively. The proximal side of the valve is shown. The white dashed line highlights the contour of the vessel. Scale bar denotes 25 μm.

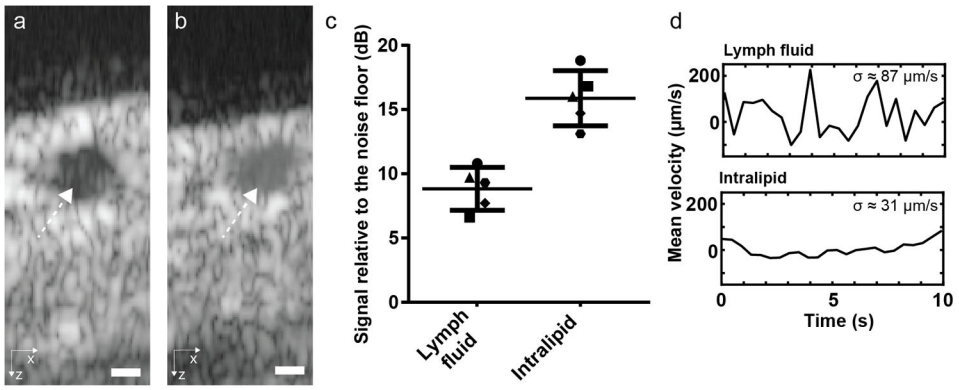

Figure 3.

Increase of the OCT signal within a lymphatic vessel after Intralipid injection. Averaged frame from the 32 repeated B-Scans at one location (a) before and (b) after the injection of Intralipid. The white dashed arrows point to the lymphatic vessel lumen. (c) The measured ratio between signal within the vessel and noise floor before and after injection across five animals shows an average SNR increase of 7 dB. (d) Doppler flow velocity curves acquired before and after injection of Intralipid show that the increased SNR improves measurement quality.

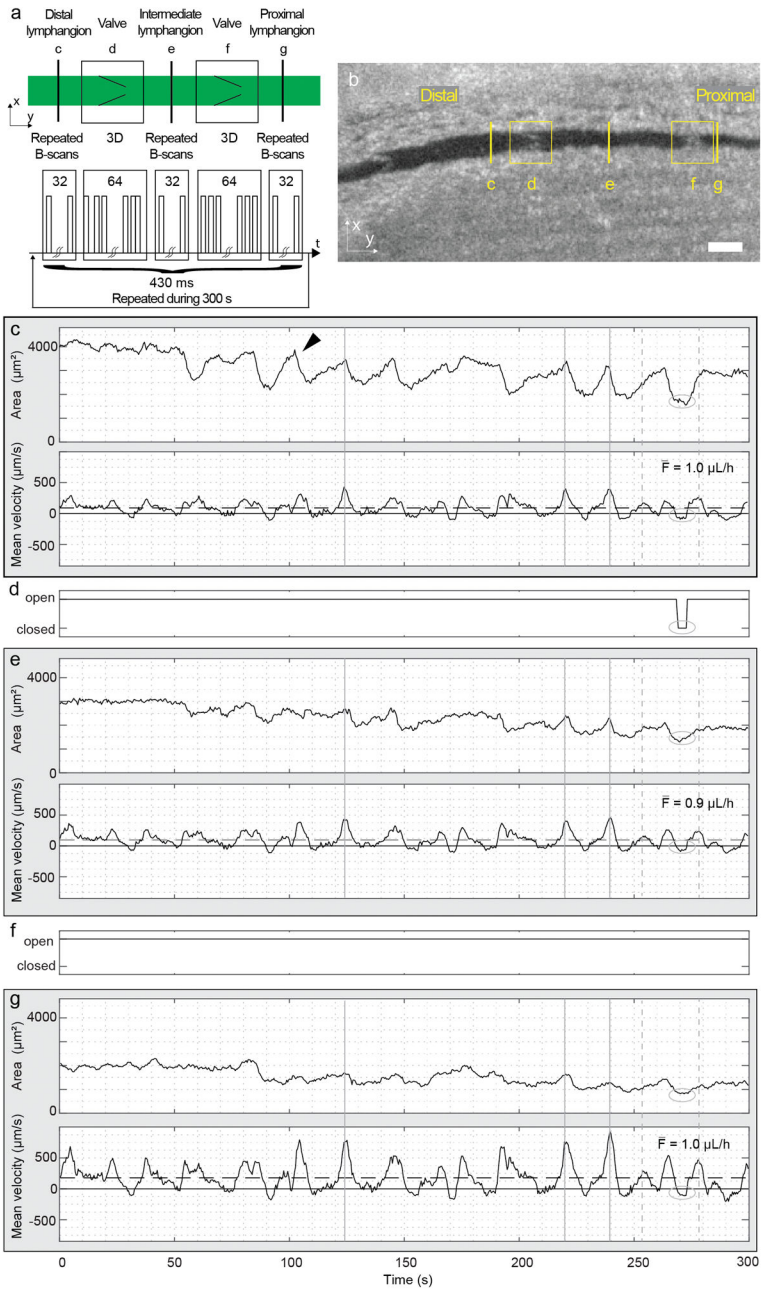

Figure 4.

Simultaneous flow measurements in three successive lymphangions and intervening valve dynamics in a normal mouse. (a) Schematic representation of the scanning pattern and timing for the simultaneous imaging at five locations. The five locations are imaged sequentially but considered simultaneous because of the short cycle duration (430 ms) compared to the flow and contractile dynamics at the imaging site. The cycle is repeated 697 times during 300 s. (b) *En face* plane crossing the lymphatic vessel extracted from the structural volume acquired with each dataset. The yellow lines highlight the anatomical locations of measurements c to g. Panels (c), (e) and (g) show measurements of the vessel

cross-sectional area (top) and mean velocity (bottom) within three lymphangions: (c) distal, (e) intermediate and (g) proximal. Arrowhead indicates an example of the beginning of a contraction. Continuous and dashed horizontal lines in the velocity plots indicate the zero and the average velocity, respectively. The average volumetric flow $\bar{F}$ over the five-minute duration is displayed. Vertical continuous and dashed gray lines are visual aids for a flow velocity pulse respectively synchronous or asynchronous to a contraction. (d) and (f) Status of the intervening valves are manually extracted from the 4D dataset. The ellipse highlights the period of the closed valve on the velocity and cross-sectional area waveforms.

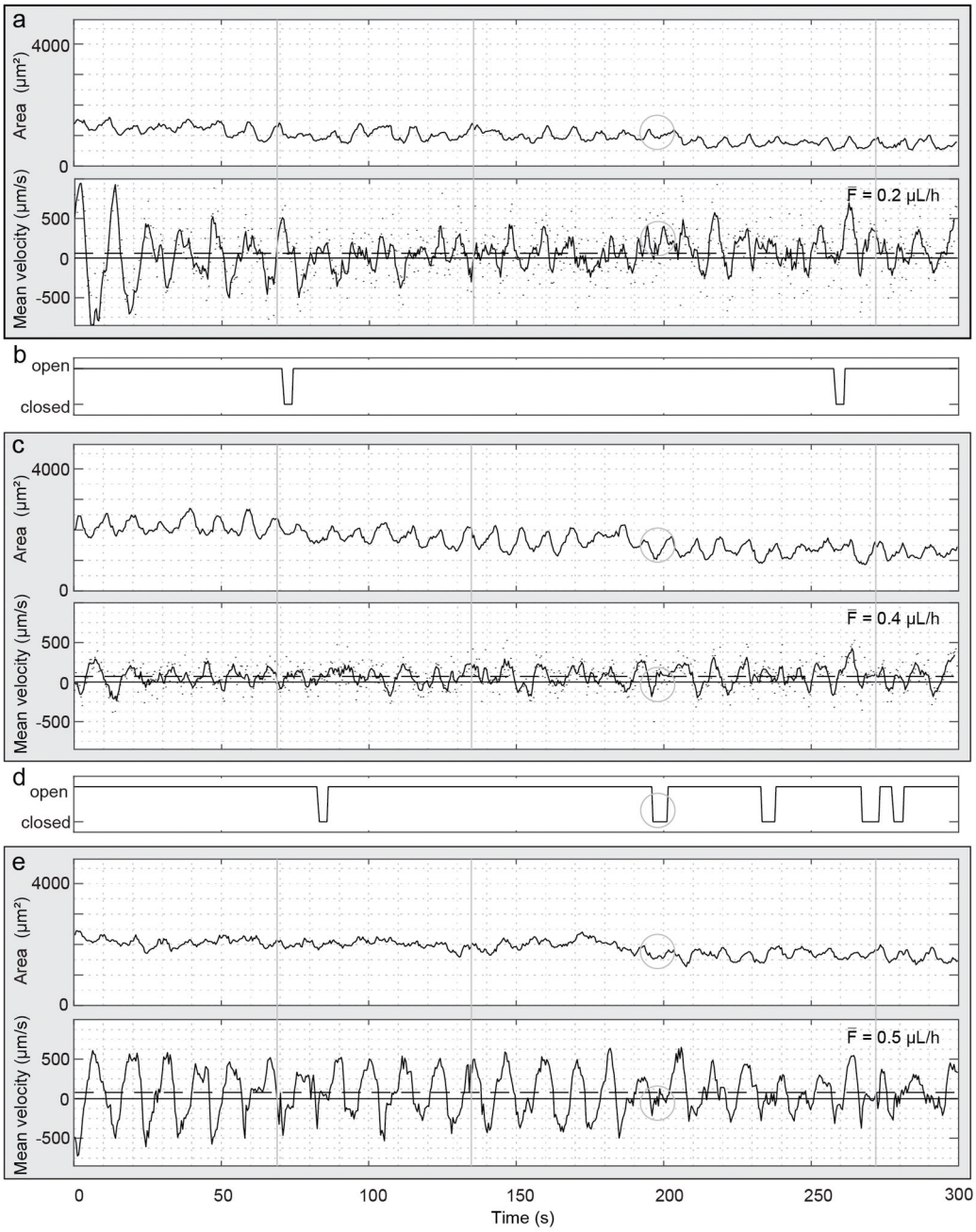

Figure 5.

Simultaneous flow measurement in three successive lymphangions and intervening valve dynamics imaging in a sterile inflammation model in a mouse. Panels (a), (c) and (e) show measurements of vessel cross-section area (top) and mean velocity (bottom) within three lymphangions: (a) distal, (c) intermediate and (e) proximal. The velocity measurements (black points) at the distal and intermediate locations were smoothed using a moving average of 4 points (solid line). The lower accuracy and precision of velocity and average flow is the result of a Doppler angle close to 90 degrees at these locations. Continuous and dashed horizontal lines in the velocity plots indicate the zero and the average velocity

respectively. The average volumetric flow $\bar{F}$ over the five-minute duration is displayed. Vertical gray lines are visual aids for synchronous contractions. (b) and (d) Status of the intervening valves manually extracted from the 4D dataset. The ellipse highlights the period of the closed valve on the velocity and cross-sectional area waveforms.

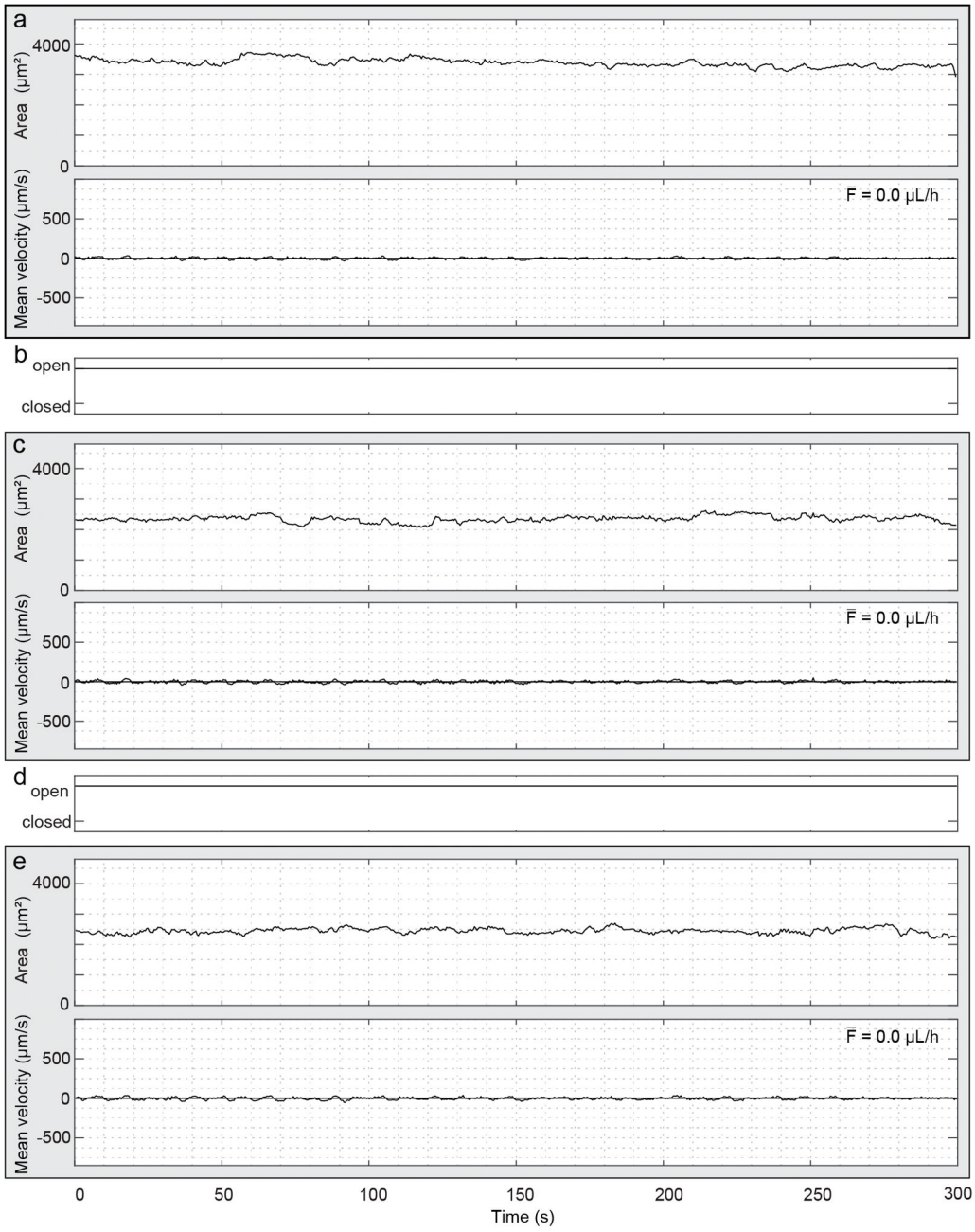

Figure 6.

Simultaneous flow measurement in three successive lymphangions and intervening valve dynamics imaging in a mouse model of inflammation. Panels (a), (c) and (e) show measurements of vessel cross-section area at the top and mean velocity at the bottom within three lymphangions: (a) distal, (c) intermediate and (e) proximal. Continuous and dashed horizontal lines in the velocity plots indicate the zero and the average velocity respectively. The average volumetric flow $\bar{F}$ over the five-minute duration is displayed. (b) and (d) Status of the intervening valves manually extracted from the 4D dataset.